

Final Draft
of the original manuscript:

Ma, S.; Yuan, H.:

Computational investigation of multi-axial damage modeling for porous sintered metals with experimental verification

In: Engineering Fracture Mechanics (2015) Elsevier

DOI: [10.1016/j.engfracmech.2015.09.049](https://doi.org/10.1016/j.engfracmech.2015.09.049)

Computational Investigation of Multi-Axial Damage Modeling for Porous Sintered Metals with Experimental Verification

Songyun Ma^a Huang Yuan^{b,*}

^a*Institute of Materials Research, Helmholtz Research Center Geesathacht, Germany*

^b*School of Aerospace Engineering, Tsinghua University, Beijing, China*

Abstract

The experimental investigation shows that the damage process in sintered metals can be divided into three stages: the elastic stage, the secondary stage and finally the tertiary stage. A phenomenological continuum damage model is introduced to predict the inelastic behavior of the sintered material and the damage process. The numerical implicit integration algorithm is developed and implemented into ABAQUS. The proposed damaged model is computationally and experimentally verified under multi-axial loading conditions. It is confirmed that the proposed damage model is able to properly describe the mechanical behavior and the damage evolution under most different loading configurations.

Key words: Sintered metals, damage evolution, continuum damage model, elastic damage, plastic damage, stress triaxiality

1 Introduction

With development of powder metallurgy (PM) technology, sintered metals have been increasingly applied to high performance parts with limited fatigue life. In automobile industry, a number of iron-based alloy sintered steels with high mechanical strength were developed for high loaded parts in order to meet requirements of lightweight design and to reduce manufacturing costs [3,36,37]. Therefore, many efforts have been devoted to investigate the damage mechanisms of sintered metals.

* Corresponding author. Email: huang.yuan@tsinghua.edu.cn

The microstructure of sintered metals is complex and heterogeneous due to irregular pores and different alloy distributions. The inherent porosity of the sintered metal is much higher than that in the conventional casting metals (Fig. 1) and varies between 8-15% [3], which results in complicated deformation and damage mechanisms. The fraction, size, distribution and morphology of the porosity directly affect mechanical properties of sintered metals. Inter-connected pore networks cause strain localizations at relatively small regions between particles, while isolated porosity induces overall deformations [34,46]. Microscopic damage mechanism of sintered metals is investigated in monotonic in-situ tensile tests [10,24]. It is found that micro-cracks always initiate in pores of which the long axis is perpendicular to the tensile direction. These micro-cracks open and/or propagate in the mode I crack direction. Straffelini et al. [39] studied the damage evolution in the sintered iron by monitoring both Young's modulus and density changes during tensile testing and argued that damage is developed in two stages: the first stage contains plastic deformations limited to pore edges, and in the second stage the bulk deformations become dominant. Chawla and Deng [13,14,18] showed that the damage developed quickly in early stage of fatigue life under relative high loading amplitude. However, most of published works focus on experimental investigation of damage mechanisms in sintered metals. A quantitative description of the inelastic damage process of sintered metals under complex loading conditions remain a major issue in view of predicting failure of sintered parts in service.

In past decades, various approaches for modeling and predicting the inelastic damage and fracture have been developed and applied to different dense materials. The Gurson-Tvergaard-Needleman (GTN) porous plasticity model, based on the work of Gurson [23], is a micro-mechanical damage model considering effects of micro-void nucleation and growth. Recently, many research efforts have been made to understand the distortion of voids and inter-void linking under shear-dominant loadings. To enhance the prediction capacity of the GTN model, additional terms containing the third stress invariant are incorporated into the porosity evolution law [2,30,43]. Danas et al. [17] proposed a homogenization-based rate-dependent plasticity model in the framework of finite strain accounting the effect the evolution of void shape on the response of material under general three dimensional loadings. Brünig et al. [7] performed micro-scale computations with the unit cell model and confirmed that the evolution of the void shape depends not only on the stress triaxiality but also on the Lode parameter, especially for the low stress triaxiality. Cao et al. [8] proposed a phenomenological lode-dependent enhanced Lemaitre model in the framework of continuum damage mechanics (CDM) to predicted fracture for both high and low stress triaxialities. Additionally, Cao et al. [9] developed a Gurson-like nonlinear homogenization-based model to capture the influence of void shape change and void rotation on the damage evolution process of ductile material at low stress triaxialities. The proposed model was verified by comparing with notched specimens and provided an accurate prediction of

damage under complex loading paths.

Due to the specialty and complexity of the sintered metal, few works on damage evolution in this kind of material have been published. Cedergren and Melin [12] extended the GTN model with the viscoplastic formulation and a combined hardening model to investigate the damage accumulation of sintered steel with 5.5% porosity under cyclic loading condition with different loading frequency. An unrealistic prediction result was obtained using the extended GTN model. Schneider and Yuan [33] applied the GTN model to the sintered iron for three different initial porosities of the material. With the material parameters from uniaxial tension, computations of notched specimens did not agree with experimental results for all investigated materials. It is concluded that the GTN model cannot directly used for the sintered metals due to the high initial porosity and the damage evolution law should be appropriately modified with respect to the different damage mechanisms in the material. Straffelini and Fontanari [38] studied the relationship between stress triaxiality and fracture strain for a ferritic-pearlitic Fe-0.4%C sintered steel and a high strength sintered steel at two porosity levels with tensile and bending tests based on smooth and notched specimens. The results showed that the Rice-Tracey fracture criterion could predict the fracture strain for the PM Fe0.4%C steels under different stress triaxialities, but overestimated the fracture strain of the high strength sintered steel. Fritzen et al. [22] concluded that the GTN model cannot capture the behaviour of highly porous material.

The essential problem in using the GTN model is quantification of the damage of sintered metals, since the sintered metal contains a high initial porosity. On the other hand, experimental studies confirm that the porosity variation of the sintered metal is very slight during its damage process [34]. The porosity in the sintered metal diminishes the material strength but is not equivalent to the material degradation. Therefore, more experimental investigations and computational studies on the damage process of sintered metals are needed to improve the predictive ability of the computational models for sintered metals under multi-axial loading conditions. Developing a micro/mechanical damage model needs detailed understanding of the damage mechanisms and quantified correlation between damage in micro/scale and macroscopic material behavior. Lacking in micro-mechanical analysis makes it difficult to generate a multi-scale based damage model. On the other hand, the phenomenological damage model based on detailed experimental observation and thermo-mechanical frame is a necessary step toward to give a more understandable description for the sintered metal.

In the present work the damage evolution in sintered iron is computationally investigated under multi-axial loading conditions, based on the experiments published in [29]. Choosing the sintered iron is to diminish effects of distributed alloy elements and to obtain higher ductility of the sintered metal. The exper-

imental investigation reveals a significant degradation in purely elastic state and increases under both tension and compression loading in the sintered metal. A phenomenological CDM model is developed based on the experimental observations to predict damage nucleation and development in the sintered iron. A damage variable is defined for describing both stress-induced damage in elastic state and plastic strain dominated damage for ductile failure, which is representing reduction of elasticity modulus in the maximum principal strain direction. The corresponding numerical implicit integration algorithm is developed and implemented into the FEM software package ABAQUS via the user interface UMAT. The strategy of the parameter identification is developed. The proposed damaged model is verified with the tubular specimens under five different proportional tension-torsion loading conditions, as well as four non-proportional loading paths. The holed specimens and notched specimens are then used to further validate the damage model under more complex stress states.

2 Continuum damage model for sintered metals

2.1 Definition of material damage

In the present work, the concept of the phenomenological continuum damage mechanics is adopted for modeling of the damage evolution in the sintered metal. Various physical mechanisms of damage of material can be considered in the framework of CDM, as reported in [19,21,28,42]. The thermodynamics framework proposed by Lemaitre is used to build the constitutive model incorporating damage for the sintered metal.

The strain rate tensor is decomposed into elastic and plastic parts as

$$\dot{\epsilon}_{ij} = \dot{\epsilon}_{ij}^e + \dot{\epsilon}_{ij}^p. \quad (1)$$

Based on the strain equivalence hypothesis of CDM, the strain associated with the damage state under a given nominal applied stress is equivalent to the strain associated with its undamaged state under the corresponding effective stress. Then, the effective stress in the undamaged configuration is defined as [27],

$$\tilde{\sigma}_{ij} = \frac{\sigma_{ij}}{(1 - D)}. \quad (2)$$

According to Lemaitre's suggestion [27], material damage can be expressed by diminishing of the elastic modulus, $D = 1 - E/E_0$, where E_0 denotes the initial elasticity modulus of the sintered metal without damage and E depending on deformations stands for actual elasticity modulus. With developing material

damage, the stiffness of the material, i.e. E modulus, decreases. Here E is determined from unloading controlled by the stress to avoid compression.

Under multiaxial loading condition, damage depends on stress/strain states. Experiments demonstrate that all specimens of the sintered iron failed along the maximum principal strain plane, which implies that micro-cracks initiate and grow along that plane. Therefore, the damage is identified by monitoring the reduction of elasticity modulus in the maximum principal strain direction in the experiments.

$$D = 1 - \frac{\hat{E}}{\hat{E}_0}. \quad (3)$$

where \hat{E} and \hat{E}_0 are the actual and initial elasticity modulus in the maximum principal strain direction, respectively. For more information on the experimental measurement of damage under tension-torsion tests, the interested reader is referred to [29].

The strain energy density release rate Y is associated to the damage variable D as follows

$$Y = \frac{1}{2} \tilde{E}_{ijkl} \epsilon_{ij}^e \epsilon_{kl}^e = \frac{\tilde{\sigma}_{eq}^2}{2E_0} f(\eta), \quad (4)$$

where $\tilde{\sigma}_{eq}$ is Mises stress according to the J_2 theory, with

$$f(\eta) = \frac{2}{3}(1 + \nu) + 3(1 - 2\nu)\eta^2. \quad (5)$$

Above $f(\eta)$ represents dependence on the stress triaxiality, η , in the energy release rate.

To fulfill the second law of thermodynamics, the Clausius-Duhem inequality under isothermal condition requires

$$\sigma_{ij} \dot{\epsilon}_{ij}^p - R\dot{r} + Y\dot{D} \geq 0. \quad (6)$$

Obeying the second law of thermodynamics, the dissipation potential function should be a convex function of internal state variables for the formulation of damage evolution law. In the next section, we postulate the dissipation potential function and deduce the evolution equations of the internal variables based on the framework of thermodynamics.

2.2 The damage evolution law

2.2.1 Additive representation of damage

Experimental observations reveal that damage in the sintered metal initiated at a very low stress level [33]. More precisely, damage of the sintered metal

can be induced by the stress, that is, the macroscopic elastic strain, before the material yields. After plasticification, the stress growth becomes secondary, whereas the damage further grows up, which is driven by the plastic strain [29]. Microscopically, since metallic particles of sintered metals are weakly linked through sintered necks surrounding by irregular pores with high stress concentrations, micro-cracks may nucleate at a lower loading level. On the other side, voids opening is accelerated by the nucleation and growth of micro-cracks. Recently, Chen et al. [15] studied the deformation mechanism of sintered iron with nanoindentation technology. They concluded that ca. 40% of the total deformations are from the void growth and micro-cracks if the overall stress is not too high. Under such consideration, the material damage is driven by both stress and plastic strain, which represent two damage mechanisms, the elastic damage induced by the microcracking and the plastic damage induced by the nucleation and growth of microvoid. The elastic damage driven by the applied stress, whereas the plastic damage dominated by the plastic strain. Due to different damage mechanisms, the damage evolution has to contain different evolution terms. Each term represents different damage mechanisms. The total damage summarizes all damages induced by the different mechanisms,

$$\dot{D} = \dot{D}_e + \dot{D}_p. \quad (7)$$

Note the decomposition of the damage does not mean to introduce two independent damage variables into the constitutive model. D_e and D_p represent two different damage mechanisms. In elastic state, the damage quickly rises with the stress, i.e. D_e must be a function of the stress. As soon as the material is plastic, the stress increment becomes smaller and diminishes gradually, i.e. \dot{D}_e vanishes, and the damage evolution is mainly controlled by the plastic strain. That is, \dot{D}_p should dominate further material degradation. Since the damage is irreversible, both \dot{D}_e and \dot{D}_p have to be positive. According to physical meaning of D , the sum of both damage variables, D_e and D_p is limited by 1.

Evolution of the different parts of damage is illustrated in Fig. 2 as a function of the equivalent strain. While D_e initiates when the stress exceeds a certain critical value, Y_0 , the plastic damage begin to nucleate beyond threshold value of plastic strain, ϵ_{th} . The material becomes unstable if damage of material reaches the critical damage value D^{cr} . Generally, ϵ_f depends on the stress triaxiality.

2.2.2 Elastic damage evolution

As defined, the elastic damage denotes the degradation of material induced by the stress. Based on the analysis of experimental results in [29], Young's modulus significantly decreases even for strain less than 0.2%, where the overall strain is still elastic. This kind of damage was known in brittle materials,

such as concrete, rocks etc. [27,41].

Figures 3(a) and (b) illustrate the damage evolution under tension and compression with the max. strain up to 1%. From Fig. 3(b) one learns that the damage initiation under uniaxial loading is characterized by the normal stress amplitude, almost independently of the stress triaxiality within a very small strain range. The compression damage nucleates at a similar loading threshold as that for the tension damage in the sintered metal, but with a lower growth rate. With increasing strain amplitude, the tension damage grows continuously, whereas the compression damage runs into the saturation quickly, see Fig. 3(a). It implies that the material can be degraded by the compressive stress, but not by the compressive plastic strain. For this reason, the elastic damage is assumed to be driven by both tension and compression and characterized by the strain energy density release rate and the plastic damage is mainly related to the tensile plastic strain.

The experimental observation implies that the elastic damage evolution can be described by the strain energy density release rate [27,41]. The potential function for the elastic damage is defined as [1]

$$F_e^D = Y - Z(D_e), \quad (8)$$

where Z is the material resistance against material damage. Y denotes the energy density release rate for material damage and is the thermodynamic conjugate variable of the stress-induced damage, D_e . Following [16] the material resistance can be expressed in the form

$$Z = Y_0 + \frac{1}{b} \ln \left(\frac{D_e^{sa}}{D_e^{sa} - D_e} \right), \quad (9)$$

where Y_0 is the initial resistance of damage and b is a model parameter. D_e^{sa} represents the saturation of the elastic damage since in elastic-plastic materials the elastic damage will not finally destroy the material but contribute to the final failure. From the maximum dissipation principle, the damage evolution law is expressed in the rate-form as

$$\dot{D}_e = \dot{\lambda}_b \frac{\partial F_e^D}{\partial Y} = \dot{\lambda}_b. \quad (10)$$

Above the damage multiplier $\dot{\lambda}_b$ is non-negative under loading/unloading conditions according to the Kuhn-Tucker relations as

$$\begin{cases} \dot{\lambda}_b \geq 0 & \text{for } F_e^D(Y, D) = 0, \\ \dot{\lambda}_b = 0 & \text{for } F_e^D(Y, D) < 0. \end{cases} \quad (11)$$

In the case of damaging, the damage multiplier $\dot{\lambda}_b$ is determined by the damage

consistency condition,

$$dF_e^D = \frac{\partial F_e^D}{\partial Y} \dot{Y} - \frac{\partial Z}{\partial D} \dot{\lambda}_b = 0. \quad (12)$$

The evolution equation of the elastic damage is expressed as

$$\dot{D}_e = D_e^{sa} b \exp[-b \langle Y - Y_0 \rangle] \dot{Y}, \quad (13)$$

where $\langle \cdot \rangle$ is the Maccauley brackets, i.e. $\langle x \rangle = (|x| + x)/2$. Obviously, the elastic damage is characterized by the initial damage resistance, Y_0 , the parameter b and the saturation damage D_e^{sa} .

The potential function in Eq. (8) predicts damage initiation and growth under a small stress level, i.e. only for elastic damage. With an increasing loading amplitude, the plastic damage is initiated and becomes more dominant. Fig. 3(b) reveals that the elastic damage goes into saturation as strain further increases. In the figure the solid curves denote predictions of the damage model introduced by the present work. The discrepancy between the elastic damage and total damage has to be overcome by the plastic damage which is related to plastic strains.

2.2.3 Plastic damage evolution

In ductile materials the damage is mainly accumulated due to plastic deformations. The plastic damage is the major fracture mode for metal failure and characterized by initiation, growth and coalescence of void due to large plastic deformations [4]. It is assumed that the plastic damage depends on both plastic strain and stress triaxiality. Recently, many research works confirmed that the Lode angle should be related to ductile failure to improve the prediction accuracy under shear-dominant loading conditions [8]. Among many CDM models developed in the past decades [6,11,25,26,44], the nonlinear CDM model proposed by Bonora [5,6] seems to be able to precisely describe the plastic damage evolution for different types of metals.

Following the concept of Bonora [5,6] the plastic damage dissipation potential F exists and there is no interaction between plasticity dissipation and damage dissipation. The total energy dissipation consists of two parts as

$$F = F_p^D + \psi_p, \quad (14)$$

where F_p^D and ψ_p are the plastic damage energy and the plastic energy dissipation, respectively. In metal plasticity, the plastic energy dissipation is generally assumed to be related to the hydrostatic stress and the Mises stress. Neglecting the volumetric compressibility, the plastic behavior of the sintered metal can be approximated by the J_2 theory. The yield function can be defined in

the nominal configuration as [1]

$$\psi_p = \tilde{\sigma}_{eq} - \tilde{\sigma}_{y0} - R(r), \quad (15)$$

where Mises stress is defined as

$$\tilde{\sigma}_{eq} = \sqrt{\frac{3}{2} \left(\frac{s_{ij}}{1-D} \right) \left(\frac{s_{ij}}{1-D} \right)} \quad (16)$$

with s_{ij} as the deviatoric stress tensor. The sintered metal is porous, i.e. the material is generally plastically compressible. In the present work, however, the main focus is at characterization of material damage, so that the plastic compressibility is neglected. The damage dissipation potential proposed by Bonora [5,6] for the plastic damage model is written as

$$F_p^D = \left[\frac{1}{2} \left(\frac{Y}{S_0} \right)^2 \frac{S_0}{1-D} \right] \frac{(D_p^{cr} - D_p)^{(\alpha-1)/\alpha}}{p^{(2+n)/n}}, \quad (17)$$

where S_0 is damage material parameter, n is the plastic hardening exponent in the Ramberg-Osgood model, α is the damage exponent that determines the shape of the damage evolution law and p is the accumulated plastic strain,

$$\dot{p} = \sqrt{\frac{2}{3} \dot{\epsilon}_{ij}^p \dot{\epsilon}_{ij}^p} \quad p = \int \dot{p} dt. \quad (18)$$

Based on the maximum dissipation principle, the evolution of internal variables can be obtained via the normality rule as

$$\begin{aligned} \dot{\epsilon}_{ij}^p &= \dot{\lambda}_p \frac{\partial F}{\partial \tilde{\sigma}_{ij}} = \dot{\lambda}_p \frac{\partial \psi_p}{\partial \tilde{\sigma}_{ij}}, \\ \dot{D}_p &= \dot{\lambda}_p \frac{\partial F}{\partial Y} = \dot{\lambda}_p \frac{\partial F_p^D}{\partial Y}, \\ \dot{r} &= \dot{\lambda}_p \frac{\partial F}{\partial R} = -\dot{\lambda}_p \frac{\partial \psi_p}{\partial R} = \dot{\lambda}_p = \dot{p}. \end{aligned} \quad (19)$$

The plastic damage process remains inactive until the effective accumulated plastic strain p reaches the threshold strain ϵ_{th} for the positive hydrostatic stress, that is,

$$\dot{D}_p = \begin{cases} 0 & \text{if } p < \epsilon_{th} \text{ or } \sigma_H < 0, \\ \frac{Y}{S_0} \frac{(D_p^{cr} - D_p)^{(\alpha-1)/\alpha}}{p^{(2+n)/n}} \dot{p} & \text{if } p \geq \epsilon_{th} \text{ and } \sigma_H \geq 0. \end{cases} \quad (20)$$

It is assumed that the plastic damage will not accumulate in the compression stress state. The comparison between experiments and predictions of the damage model are summarized in Fig. 3. The model parameters are identified in the next section. From the figures the present model can predict the damage initiation and growth reasonably.

3 Numerical implementation

3.1 Update of stresses and state variables

An effective and reliable integration algorithm of differential equations is required to incorporate the constitutive model into the commercial FEM software ABAQUS. The differential equations of the constitutive model have to be numerically solved for each Gaussian point in the nonlinear computation procedure. In this section, an implicit implementation strategy is summarized based on the backward Euler scheme. The local integration algorithm is devoted to update the internal state variables and stresses to the present loading configuration for the given strain increment by using the Newton-Raphson method. The details for building the tangent operator of the implicit integration algorithm are summarized in Appendix 5. As known, material softening induced by material degradation will cause convergence difficulties and lead to interruption of computation. For this reason, the viscous regulation method is used to improve convergence.

The update procedure for the stress and state variables consists of three steps: elastic prediction, plastic correction and damage correction based on the widely used return mapping method, which has been applied to develop an integration algorithm for various constitutive models with a high efficiency [1,16]. In the elastic prediction step, the internal state variable are not changed and the stress is updated elastically, where the plastic deformation and damage evolution are frozen. In the case of satisfaction of the yield condition, the plastic corrector step has to be activated and the Newton-Raphson method is used to iteratively solve the effective stress and plastic strain increments for the Gaussian point. With the updated effective stress and equivalent plastic strain, the elastic damage and the plastic damage should be computed according to the damage evolution equations. Finally, the stress at actual time $t + \Delta t$ is obtained based on the updated effective stress, plastic strain and damage values.

The effective stress in the undamaged configuration can be calculate with damage value and stresses at the time t as

$$\tilde{\sigma}_{ij}^t = \frac{\sigma_{ij}^t}{1 - D^t}. \quad (21)$$

The superscript t denotes the previous incremental step here. All variables without superscript mean the current values at time $t + \Delta t$. In the elastic prediction step, the effective trial deviatoric and Mises stress can be calculated

with Hooke's law,

$$\begin{aligned}\tilde{s}_{ij}^{tr} &= \frac{s_{ij}^t + 2G\Delta e_{ij}}{1 - D^t}, \\ \tilde{\sigma}_{ij}^{tr} &= \tilde{\sigma}_{ij}^t + \tilde{E}_{ijkl}\Delta\epsilon_{kl}, \\ \tilde{\sigma}_{eq}^{tr} &= \sqrt{\frac{3}{2}\tilde{s}_{ij}^{tr}\tilde{s}_{ij}^{tr}},\end{aligned}\tag{22}$$

where $e_{ij} = \epsilon_{ij} - \delta_{ij}\epsilon_{kk}/3$ denotes the deviatoric strain tensor. \tilde{E}_{ijkl} represents the actual elastic stiffness tensor. The superscript "tr" stands for the elastic trial of the variable. Obviously, all terms above are known without accounting for yield condition. In the plastic correction step the yield condition has to be considered and the plastic strain increment within the frame of the J_2 formulation is to be evaluated from

$$\Delta\epsilon_{ij}^p = \Delta p \frac{\partial\psi_p}{\partial\tilde{\sigma}_{ij}^{tr}} = \Delta p \frac{\tilde{s}_{ij}^{tr}}{\tilde{\sigma}_{eq}^{tr}} = \Delta p \frac{\tilde{s}_{ij}^{tr}}{\tilde{\sigma}_{eq}^{tr}},\tag{23}$$

where the equivalent plastic strain increment is defined as

$$\Delta p = \sqrt{\frac{2}{3}\Delta\epsilon_{ij}^p\Delta\epsilon_{ij}^p}.\tag{24}$$

If the plastic strain hardening is nonlinear, the equivalent plastic strain increment has to be solved by the Newton-Raphson method. The yield function in the J_2 theory incorporating damage is defined as

$$\psi_p = \sqrt{\frac{3}{2}\frac{\tilde{s}_{ij}^{tr}}{(1-D)}\frac{\tilde{s}_{ij}^{tr}}{(1-D)}} - \sigma_y(p) = 0\tag{25}$$

with σ_y as yield stress as a function of the equivalent plastic strain p . It can be simplified with the trial Mises stress, $\tilde{\sigma}_{ep}^{tr}$, as

$$\psi_p = \tilde{\sigma}_{ep}^{tr} - 3G\Delta p - \sigma_y(p^t + \Delta p) = 0.\tag{26}$$

Above the equivalent plastic strain increment Δp has to be iteratively solved using the Newton-Raphson method.

With the updated equivalent plastic strain increment, Δp , the yield stress at the time $t + \Delta t$ can be calculated with the corresponding stress-strain relationship, e.g. in the form of the Ramberg-Osgood model. The effective stress at the current time can be updated as

$$\tilde{\sigma}_{ij} = \frac{\tilde{s}_{ij}^{tr}}{\tilde{\sigma}_{eq}^{tr}}\sigma_y + \frac{1}{3}\delta_{ij}\tilde{\sigma}_{kk}^{tr}.\tag{27}$$

In the stress integration algorithm above, the damage evolution is not considered, that is, the damage is assumed to be constant. In the damage correction step, the damage driving force Y at the time $t + \Delta t$ can be directly obtained from the following equation,

$$Y = \frac{(\tilde{\sigma}_{eq})^2}{2E_0} f(\eta). \quad (28)$$

The elastic damage is activated if the criterion

$$F_e^D = Y - Z(D_e^t) > 0 \quad (29)$$

is satisfied and the elastic damage can be updated from

$$\Delta D_e = D_e^{sa} \{1 - \exp[-b < Y - Y_0 >]\} \Delta Y. \quad (30)$$

The plastic damage part can be written in the incremental form with the backward Euler integration scheme as

$$\Delta D_p = \begin{cases} 0 & \text{if } p < \epsilon_{th} \text{ or } \sigma_H < 0, \\ \frac{Y}{S_0} \frac{(D_p^{cr} - D_p^t - \Delta D_p)^{(\alpha-1)/\alpha}}{p^{(2+n)/n}} \Delta p & \text{if } p \geq \epsilon_{th} \text{ and } \sigma_H \geq 0. \end{cases} \quad (31)$$

Note the above evolution equation for the plastic damage is nonlinear about ΔD_p . Updating ΔD_p has to be performed iteratively by using the Newton-Raphson method. The total damage is obtained from $D = D^t + \Delta D$ with $\Delta D = \Delta D_e + \Delta D_p$. Finally, the stress in the damaged configuration is calculated from the effective stress and damage values as

$$\sigma_{ij} = (1 - D)\tilde{\sigma}_{ij}. \quad (32)$$

3.2 Treatment of the damage variable beyond the critical damage

In the experiment it is observed that the stress-strain curve did not display obvious softening and specimens did not show necking before fracture. As discussed in the previous section, the material rapidly loses its loading capacity, that is, D grows to 1 quickly if the critical damage value is exceeded. On the other side, the FEM element does not fail if the damage variable only at one Gaussian point reaches the critical damage value. Furthermore, in the implicit computation the element can not be simply removed even if the damage values of all corresponding Gaussian points in the element exceed the critical damage. Otherwise, it will cause non-convergence in the computation. For this reason,

the plastic damage beyond the critical damage has to be modified as

$$\begin{cases} \dot{D}_p = \beta \langle \dot{\epsilon}_1 \rangle & \text{for } D_p > D_p^{cr}, \\ D_p = \min(D_p, D_f). \end{cases} \quad (33)$$

Above β is a large value for modeling rapid degradation of material and can be calibrated by simulating the softening behavior of material in uniaxial tensile test. In the present work $\beta = 15$ is set based on extensive computational experiments. $\dot{\epsilon}_1$ its maximum principal strain increment. The second equation above is used to limit the increasing of D to improve convergence of numerical integration. Generally, the maximum value of damage D_f is set less than 1 to remain small stiffness of the element. Effects of the D_f have been numerically experimented. It is confirmed that the final value of D_f affects computational very slightly if $D_f \geq 0.9$. The computational convergence becomes worse with a larger D_f . In the present work $D_f=0.9$ is assumed for further computations.

4 Computational verifications

4.1 Identification of model parameters

For complex material models the parameter identification is a tricky task. In the present work the parameters of the CDM model should be identified from uniaxial tensile and compression tests. Experiments under multi-axial and complex loading conditions are used to validate the CDM model. As reported in the previous section, the damage rapidly grows in the very small strain range and it implies that the elastic damage may dominate the material behavior in the elastic state. Under compressive loading condition, Fig. 3 shows that the damage reaches a saturated stage for large compressive loads. It implies that the compressive plastic strain does not contribute to material degradation and the plastic damage will not accumulate in the pure compressive stress state. This experimental observation suggests that the model parameters for the elastic damage evolution can be identified in the compression test. The plastic damage evolution law can then be obtained from uniaxial tensile tests, in which the plastic damage denotes the difference between the total damage and the elastic damage, i.e.

$$D_p = D - D_e. \quad (34)$$

In the computation, the stress-strain curve in the undamaged configuration is needed to describe the hardening behavior of material and is assumed to be represented by the Ramberg-Osgood model. The experimental tensile test

provides the stress-strain curve coupled with damage. However, the stress-strain curve for the undamaged material can be evaluated with the effective stress concept for the uniaxial stress state and can be expressed as a function of plastic strain as

$$\tilde{\sigma}_{ij} = \frac{\sigma_{ij}}{(1-D)} = Kp^{1/n}, \quad (35)$$

where the damage variable, D , has been measured by monitoring variations of the actual elastic modulus under tension. The identification of the damage evolution law should provide an optimal agreement between experimental results and model predictions for various loading cases.

The details of the identification procedure for the material parameters in the proposed damage model using uniaxial tensile and compression tests were reported in [29]. The material parameters of the elastic-plastic damage model for sintered iron are summarized in Table 1.

4.2 Computations

The developed damage model for the sintered metal is implemented into the FEM software ABAQUS via user subroutine UMAT using the proposed numerical algorithms. Computational simulations of experiments are performed to verify the damage model. An axisymmetric model with torsion is built for the tubular specimen, see Fig. 4(a). Five proportional loading paths (Fig. 4(b)) and two non-proportional paths are adopted to examine the prediction ability of the proposed damage model under multi-axial loading conditions.

The holed specimens with two different diameters and a notched specimen (Fig. 5) are used to verify the damage model under more complex loading conditions with stress gradients. The results of the computations are compared with the experimental data and analytical solutions for the detailed understanding of the proposed damage model.

4.3 Mesh dependency of computation results

It is known that a constitutive model incorporating strain softening will cause mesh-dependence in computations. Different techniques have been proposed to overcome this problem, such as nonlocal treatment, gradient-dependent model and viscous regularization [31,32,40,45]. Due to its simplification in the implementation, the viscous regularization method is incorporated into the present damage model to reduce damage localization and improve convergence [31], which is a generalization of the Duvaut-Lions viscoplasticity regularization model. In this method the strain rate dependence is introduced

into the damage evolution law. The basic idea of viscous regularization is that the softer element with damage will be stiffer due to higher strain rate in the element, which is resulted from strain localization within the element [31]. For sufficiently small time increments, the tangent stiffness matrix of the softened material is positive definite [20]. The viscous regularization scheme is formulated in the following form

$$\frac{dD^v}{dt} = \dot{D}^v = \frac{1}{\xi}(D - D^v), \quad (36)$$

where ξ is the viscosity coefficient and D^v is a viscous damage replacing the damage variable D in the constitutive equations. The viscous damage at time $t + \Delta t$ can be obtained using the backward Euler scheme from Eq. (36),

$$D^v = \frac{\Delta t}{\xi + \Delta t}D + \frac{\xi}{\xi + \Delta t}D_t^v, \quad (37)$$

where D_t^v is the viscous damage value at time t . For $\xi = 0$, the viscous damage recovers to damage without viscous effect. The disadvantage of viscous regularization method is to add artificial viscous effect into the damage evolution law. For this reason, the viscosity coefficient ξ should be small enough to reduce the artificial effect. In the work the viscosity coefficient is chosen to be 0.0002 after extensive computational efforts.

The computational results with different element sizes are shown in Fig. 6. As known, the specimen loading capacity decreases with the reducing element size. However, the mesh dependency becomes insignificant if the mesh is fine enough due to the viscous regularization, which implies that the mesh fineness has to reach a certain level to generate a unique computation. In the present work the mesh-dependency is neglected if the maximum deviation of the loading-displacement curve is smaller than 5%.

4.4 Computations of tubular specimens under proportional loading

4.4.1 Simulation results of the proposed damage model

The CDM model has been identified in the uniaxial tests. The model parameters will be applied to predict damage evolution under tension-torsion loading in the present section. Effects of the multi-axial loading have to be studied in the tubular specimen. For the tubular specimen, axisymmetric elements with twist, CGAX8, in ABAQUS can be used for studying tension-torsion effects with 5 different loading paths. The axial displacement and twist angle is applied to the upper edge of the specimen. Effects of loading mixity and loading proportionality are investigated experimentally and computationally.

Comparison between the computational prediction and the experimental data for the tension-torsion tests under proportional loadings is plotted in Fig. 7. For each loading path, two specimens were used to conduct the testing, so that the repeatability of the test is ensured. The average data is used to compare with computational results. In Fig. 7(a) the Mises stress ($\sigma_{eq} = \sqrt{\frac{3}{2}s_{ij}s_{ij}}$) is plot versus equivalent strain ($\epsilon_{eq} = \sqrt{\frac{2}{3}\epsilon_{ij}\epsilon_{ij}}$) for five loading paths. It is seen that the computational results well coincide with experimental results until 10 % strain. Obvious deviations are observed for large strain ranges. It implies that the J_2 plasticity model might be not accurate for the sintered metal with large deformations. As stated previously, the present computations neglected plastic compressibility of the sintered metal.

In Fig. 7(b) the damage evolutions from both computations and experiments are summarized. Small deviations are found for pure torsion in $\epsilon_{eq} < 0.1$, whereas all other loading paths show reasonable agreement. Since the model parameters were identified under pure tension/compression, more significant deviations for torsion seem acceptable due to anisotropy of damage. In addition, the curves show the trend that more torsion leads to an increase of the over-prediction of experimental results. However, the simulation curve of the pure torsion loading underestimates the experimental results. This may be caused by too high damage in the early loading stage (see Fig. 7(b)) leading to smaller stresses.

In general the present CDM model does provide an acceptable description of the damage evolution in the sintered material under general tension-torsion proportional loading conditions although the damage is assumed to be isotropic. However, an anisotropic damage model or an improvement of damage evolution equation incorporating the stress triaxiality can help to achieve a more accurate description of damage process in sintered metals.

4.4.2 Comparison with Lemaitre models

In order to validate the prediction capacity of the present damage model for the sintered metal, the present damage model is compared with the Lemaitre damage model [27] as well as the lode-dependent enhanced Lemaitre model proposed by Cao [8], together with the experimental data. The damage evolution equation in the Lemaitre damage model is expressed in rate from as

$$\dot{D} = \left(\frac{Y}{S_0}\right)^s \dot{p}, \quad (38)$$

where s and S_0 are two material parameters, which can be identified from uniaxial tension test. The strain energy density release rate Y is defined in Eq. (4). The Lemaitre damage model has been widely used to model damage of dense metallic materials.

Recently, Cao [8] extended the Lemaitre damage model by introducing the Lode parameter into damage evolution equation in order to account for the influence of the third stress invariant on the fracture of material as

$$\dot{D} = \left(\frac{Y}{S_0}\right)^s \frac{1}{\alpha_1 + \alpha_2 \bar{\theta}^2} \dot{p} \quad (39)$$

where α_1 and α_2 are two material parameters related shear damage. The Lode parameter $\bar{\theta}$ is defined as

$$\bar{\theta} = 1 - \frac{2}{\pi} \arccos \left(\frac{27}{2} \frac{J_3}{(\sqrt{3}J_2)^3} \right), \quad -1 \leq \bar{\theta} \leq 1 \quad (40)$$

where J_2 and J_3 are the second and third invariant of the deviatoric stress tensor, respectively. With the choice of $\alpha_2 = 1 - \alpha_1$ the original Lemaitre model is resumed in the case of uniaxial tension with $\bar{\theta} = 1$.

The model parameters s and S_0 are identified by fitting the damage evolution curve in the uniaxial tension test. In the experiments, we observed that the damage threshold strain of sintered metals is below 0.5% under all investigated loading cases due to the presence of an initial void with the irregular shape in the microstructure, which accelerates the damage initiation under loading. The influence of the damage threshold strain on the application of Cao and Lemaitre models in sintered metals is very limited. Therefore, we neglect the damage threshold strain. Neglecting the damage threshold strain, the damage evolution equation can be obtained by integrating Eq. (38) and combining Eq. (4) and (35),

$$D = \left(\frac{K^2}{2ES_0}\right)^s \frac{2s+n}{n} p^{\frac{2s+n}{n}}. \quad (41)$$

With $s = -1.177$ and $S_0 = 0.318$, the Lemaitre model can reproduce the damage evolution curve in the uniaxial tension test as shown in Fig. 8(a). Under proportional loading conditions, the equivalent plastic strain leading to fracture of material p_{cr} can be written as

$$p_{cr} = \left[\left(\frac{K^2 f(\eta)}{2ES_0}\right)^{-s} D_p^{cr} g(\bar{\theta}) \frac{2s+n}{n} \right]^{\frac{n}{2s+n}}, \quad (42)$$

where $f(\eta)$ is defined in Eq. (5) and D_p^{cr} is the critical damage value. $g(\bar{\theta})$ is related to the effect of Lode parameter on the fracture of material

$$g(\bar{\theta}) = \begin{cases} \frac{1}{\alpha_1 + \alpha_2 \bar{\theta}^2} & \text{(Modified Lemaitre model)} \\ 1 & \text{(Lemaitre model)}. \end{cases} \quad (43)$$

The predicted fracture plastic strain by the Lemaitre model, the modified Lemaitre model and the present damage model under different proportional

loading conditions are displayed in Fig. 8(b), in which the solid symbols denote experiments and open symbols are computations. The analytical solution is obtained from the CDM model under tension-torsion loading condition with constant stresses and strains over the whole specimen. The analytical prediction based on the parameter set for the tension tests is plotted together with the experimental data for various loading configurations in Fig. 8(b). The fracture strain for the FEM computations is taken where the Mises stress drop to 90% of maximum Mises stress in the loading history. From the figure one sees rather good agreement between the analytical prediction of the proposed damage model and experiments. Only at $\sigma_H/\sigma_{eq} \approx 0.26$ and 0.16 there are small discrepancy, which could be caused by irregularities in the specimens.

Apparently, the Lemaitre model can not capture the influence of the multi-axial stress on the fracture behavior of the sintered metal. In contrast, the modified Lemaitre model can properly predict the fracture strain of the sintered metal under proportional loading conditions with the best fitting parameters $\alpha_1 = 2$ and $\alpha_2 = 1 - \alpha_1 = -1$. It is noted that the material parameter set $\alpha_1 = 2$, $\alpha_2 = -1$ lead to a positive term of $g(\bar{\theta})$ and the positive damage rate due to $-1 \leq \bar{\theta} \leq 1$. More details of the comparison of different models are illustrated in Fig. 8(c), in which the relative error is evaluated by error = $(p^{pre} - p^{exp})/p^{exp} \times 100\%$, where p^{pre} and p^{exp} are the predicted and experimental fracture plastic strain, respectively. It is seen that the proposed damage model can properly predict the fracture plastic strain for all studied loading path with a relative error smaller than 15%.

4.5 Damage evolution under non-proportional loading

The effect of non-proportional loading on the damage evolution process of sintered iron is experimentally and computationally investigated in the present section. Different non-proportional loading paths are compared, as shown in Fig. 9 (a). The non-proportional loading consists of several tension-torsion or torsion-tension cycles. The equivalent strain increment of each cycle increases with the loading, $\Delta\epsilon = 0.5\%, 1\%, 2\%, 3\%$ and 4% so on until the specimen is broken. The corresponding proportional loading ratio is set to $\epsilon/\gamma = 1.5$. At the end of each cycle the specimen is unloaded to investigate damage evolution (Fig. 9(b)) with the same method described for the proportional loading cases. In the experiment it is observed the specimens were broken in the tension stage for both non-proportional cases.

For proportional loading case the stress triaxiality is nearly constant during whole loading history. In the non-proportional tests the stress triaxiality varies with loading paths, as shown in Fig. 11. Experiments reveal that the loading proportionality affects the loading capacity of the sintered iron slightly, as

shown Fig 10(a). The symbols denote experimental data. It is noted that the discrepancy between computational and experimental results is limited within small strain range 1%, since the stress-strain curve from the experiment contains Lüder-band and the stress-strain curve for computation is fitted by the Ramberg-Osgood model. The tension seems more severe for damage evolution, so that the tension-torsion loading path possesses the lower loading capacity than the loading torsion-tension. The latter agrees with the proportional loading result. It can be further found the damage under tension-torsion loading is slightly larger than that under torsion-tension in damage evolution (Fig 10(b)). Comparing with the corresponding proportional test, the deviations from non-proportional loading are small.

Computational prediction based on the same parameter set as in the previous sections is plotted in solid lines in Fig. 10. It confirms that the small effects of the loading proportionality can be captured by the present CDM model properly. From this point of view, the non-proportional loading does not influence the overall behavior of the sintered iron.

Variations of the stresses in the non-proportional strain increments are summarized in Fig. 11(a). Due to the step function of the strains, the stresses vary cyclically. The sudden changes of the loading directions cause the swaying of the stresses. Whereas the tension-torsion loading decreases the normal stress and so the stress triaxiality η . The variations of the stress triaxiality is summarized in Fig. 11(b).

Generally speaking, no significant damage is additionally induced by the tension-torsion non-proportional loading. Damage evolution of the sintered iron seems not sensitive to the tension-torsion non-proportional loading path. The proposed constitutive model is able to reasonably predict damage evolution and inelastic deformations under different used loading paths. More validation of the proposed damage model under non-proportional loading paths can be performed by simulating the complex forming processes.

4.6 *Damage in holed specimens*

To study effects of the specimen geometry to damage evolution, holed specimens with diameters of 2mm and 3mm have been investigated in the present section. The geometry details of the holed specimen are shown in Fig. 5(a). 3D computations are performed for the holed specimens. Since the holed specimen is symmetric, the FE model corresponds to the upper-right eighth of the gauge section as illustrated in Fig. 12. The vertical displacement is applied to the upper surface as loading.

The damage distribution on the 3D specimen is illustrated in Fig. 12 for

the holed specimen with the diameter of 3mm. The contour plots show the distribution of damage at three different stages of loading. The maximum value of damage appears at the middle of the hole root, where the stress triaxiality and effective plastic strain are highest. Then, the damage spreads over the thickness toward the outer surface of specimen. In the same time, the damage propagates in the ligament.

In Fig. 13, the damage evolution process in two locations is documented. the location A is at the symmetric plane near the hole root, whereas the location B is in the free surface. The elastic damage at A and B seems to be similar, as shown in Fig. 13. Under elastic loading condition, the stress triaxiality at A differs from that at B not so strong that affects damage evolution. This phenomena is also observed in the other holed specimen with a diameter of 2mm. A significant difference is found in the plastic damage growth rate. Due to the higher stress triaxiality at A the plastic damage grows much more quickly than that at B. It follows that the crack nucleates at the middle plane of the specimen at first.

Figure 14 shows the load-displacement curves for the two holed tensile specimens with diameters of 2mm and 3mm. For the each diameter three specimens have been tested. Experimental data are plotted in the figure. The holed specimens were bored after sintering, so that the effect of the hole drilling is unaccountable. As well known, the sintered iron is weak and can be deformed/damaged at a lower loading level. The machining effect is more obvious in the specimens with the larger hole. Therefore, the experiments display obvious scattering, especially for the specimens with the 3mm hole.

The lines in Fig. 14 are FE computations with and without damage modeling. The model parameters are identified in the uniaxial tests, as discussed in the previous sections. As expected, the J_2 plasticity cannot account for damage-induced structure softening and predicts an increasing loading capacity. Without damage the computational results predicts stiffer response of material at large displacement. The computations based on the proposed CDM model give acceptable results to account for structural softening. Due to elastic damage, discrepancy between the J_2 plasticity and the present CDM is obvious even at low loading stage.

4.7 *Damage in notched specimens*

The notched specimen (Fig. 5(b)) is directly fabricated by compacting and sintering without machining. Due to its geometrical symmetry, only one eighth of the specimen has to be modeled. The same model parameter set as in the previous examples has been used here. The force-displacement curves from

computations are in good agreement with the experimental curve, as shown in Fig. 15. The hardening and softening behavior of specimen in the experiments can be well predicted by the FEM computation. The computational prediction without damage over-estimated the load, even in the small displacement level. It confirms that the damage occurred at the low loading level should be taken into account to obtain an accurate computational result, which is consistent with introducing elastic damage into the damage evolution law.

In order to better understand the failure mechanisms, the fracture surface of the notched specimen was examined with the scanning electron microscope (SEM). It is found that the inherent porosity exists in a complex interconnected manner. Many ductile dimples can be observed in the necks between particles beside inherent porosity. The necks are the weakest area in the cross section. The interconnection of ductile dimples in the sintered neck regions leads to final fracture of the specimen. No trans-particle fracture was found in the SEM analysis. The geometry of inherent pores are larger than the ductile dimples.

The damage evolution process in two different locations is illustrated in Fig. 17. The results denote that damage was initiated on the subsurface near the notch root at the specimen symmetric plane (location A) where stress triaxiality is highest. Damage propagated through the specimen thickness to the surface (location B). Near the middle plane of the specimen, the damage is dominated by the high stress triaxiality and the crack propagation remains in the symmetric plane of the whole specimen. Near the free surface of the specimen, however, the damage evolution is influenced by the out-of-plane shear stress. The crack near the free surface develops under the I & III mixed-mode loading condition, as observed in experiments. Finally, the fracture surface of the notched specimen is mixed by normal failure in the specimen center and slant fracture near the surface (Fig. 17). To understand the feature of the fracture or the damage evolution process, the contour of effective plastic strain and stress triaxiality are plotted in Fig. 18. It is shown that higher damage area is a result of both strain effective plastic strain and stress triaxiality. However, the contour of damage is more similar with effective plastic strain. This means, the plastic strain is more dominant than the stress triaxiality in this case.

In Fig. 19 damage contours on the free surface between experiments and FEM computations are compared to evaluate the prediction ability of the computation. The damage contours of the specimen is captured under microscope, after the specimen experiences 90% of maximum displacement determined in experiment, at which the experiment was stopped without breaking. It is seen that there are many small cracks and voids on the surface of specimen at this loading level. The most damaged area on the surface is near the notch, whereas the damage in the middle of surface is significantly limited. The computational results predict accurately the distribution of damage on the surface

of specimen, as shown in Fig. 19.

5 Discussions and Conclusions

In the present work the damage evolution of the porous sintered iron is investigated experimentally and computationally under multi-axial loading conditions. The initial porosity of the material is ca. 8%. A new continuum damage model is proposed for the porous sintered metals. Furthermore, an implicit integration algorithm is developed for the proposed damage model and implemented in the finite element code ABAQUS. The proposed damage model is verified experimentally in different specimens and loading paths. The proposed damage model considers two different damage mechanisms of sintered metals by separating the damage into the elastic and plastic damage parts based on experimental observations. In sintered metals, the growth of porosity diminishes the material strength but is not equivalent to the material degradation. Therefore, the proposed damage model has a simple form without introducing the Lode-parameter, which is crucial for considering the void shape evolution and rotation at low stress triaxialities. However, the results show that the proposed damage model is able to reasonably predict the mechanical response of sintered metals under proportion and non-proportional loading conditions. Based on both experimental and computational discussions the following conclusions can be drawn:

- Experiment results confirm that the damage of sintered porous metal initiates at a very small strain range. The degradation of material occurs at much lower load level than the yield stress. The damage affects the structural stiffness, as shown in the notched specimens.
- The proposed CDM model assumes that the damage is isotropic, although experiments confirm that the damage evolution in the tension differs from that under torsional. The sintered metals seem more tolerant for torsion loading than the for the tensile loading.
- The damage evolution is identified for describing degradation of material stiffness and can be decomposed into two parts, the stress-induced damage (the elastic damage) and the plastic strain-induced damage (the plastic damage), in which the elastic damage is determined by the stress or elastic strain and the plastic damage is driven by the plastic deformation. The evolution equations for both damage variables have been developed within the framework of thermodynamics. The procedure for identification of model parameters is established based on uniaxial tension and compression tests.
- Predictions from the CDM model have been experimentally and computationally verified in different specimens and loading configurations. Although the damage variable is assumed to be isotropic, a good agreement between the experimental results and computational predictions builds reliable ba-

sis for further applications of the CDM model for more complex structure analysis. The prediction of material response of the sintered metal at large strains may be improved by using compression-dependent yield function.

- Experiments reveal significant variations of fracture strain with loading configuration, which can be predicted quite precisely by the present damage model and further verified by the FEM computations.
- No additional damage variable is necessary for non-proportional loading configuration, the damage evolution in the sintered metal is insensitive to the loading proportionality.

The proposed damage model in the present work is phenomenological, no micro structural effects of the sintered metals have been considered. The difficulty for a micro mechanical model is in creating a theoretical microscopic model for the complex sintered particles. Morphology of the sintered metals is substantial but complicated for developing a micro mechanical model. Additionally, the present CDM model cannot be applied for fatigue directly. The cyclic accumulative damage differs from the monotonic damage mechanism studied in the present work. The damage evolution has to be renewed essentially for considering fatigue damage in the sintered metals.

Acknowledgement:

This work was supported by the National Natural Science Foundation of China (Grant No. 51175041). The authors have to express the deep acknowledge to the GKN sinter metals for providing interesting sintered metals and to Dr. Markus Schneider of GKN for the interesting discussions.

Appendix A: Consistent algorithms operator

With application of Newton-Raphson method for solving the global the non-linear equations in the FEM computation, the rate of convergence is strongly dependent on the applied elasto-plastic tangent stiffness [1,16]. To guarantee the quadratic convergence, the algorithmic tangent stiffness should be consistent with the updating algorithm of stress and internal state variables. The procedure to derive consistent algorithms operator is followed the guidelines of Simo and Hughes [35].

Differentiating the stress updating equation,

$$\sigma_{ij} = (1 - D^n)\tilde{\sigma}_{ij}, \quad (44)$$

one obtains

$$\dot{\sigma}_{ij} = (1 - D^v)\dot{\tilde{\sigma}}_{ij} - \tilde{\sigma}_{ij}\dot{D}^v. \quad (45)$$

Applying the derivative of Eq. (45) with respect to the strain tensor, the consistent tangent operator can be written as

$$\frac{\partial \sigma_{ij}}{\partial \epsilon_{kl}} = (1 - D^v) \frac{\partial \tilde{\sigma}_{ij}}{\partial \epsilon_{kl}} - \tilde{\sigma}_{ij} \otimes \frac{\partial D^v}{\partial D} \left(\frac{\partial D_e}{\partial \epsilon_{kl}} + \frac{\partial D_p}{\partial \epsilon_{kl}} \right). \quad (46)$$

According to Eq. (37), we have

$$\frac{\partial D^v}{\partial D} = \frac{\Delta t}{\xi + \Delta t} \quad (47)$$

The derivative of elastic damage respect to the strain tensor can be rewritten as

$$\frac{\partial D_e}{\partial \epsilon_{kl}} = \frac{\partial D_e}{\partial \epsilon_{mn}^e} \frac{\partial \epsilon_{mn}^e}{\partial \epsilon_{kl}}. \quad (48)$$

With Hooke's law, the derivative of the elastic strain tensor respect to the strain tensor can be rewritten as

$$\frac{\partial \epsilon_{mn}^e}{\partial \epsilon_{kl}} = \tilde{E}_{mnpq}^{-1} \frac{\partial \tilde{\sigma}_{pq}}{\partial \epsilon_{kl}}. \quad (49)$$

With Eq. (30) and Eq. (4), the derivative of elastic damage respect to elastic strain tensor is

$$\frac{\partial D_e}{\partial \epsilon_{mn}^e} = \frac{\partial D_e}{\partial Y} \frac{\partial Y}{\partial \epsilon_{mn}^e} = D_e^{sa} b \exp[-b \langle Y - Y_0 \rangle] \tilde{\sigma}_{mn}. \quad (50)$$

Equation (31) can be rewritten as

$$F = D_p - D_p^n - \frac{Y}{S_0} (D_p^{cr} - D_p)^{\frac{\alpha-1}{\alpha}} \frac{\Delta p}{p^{(2+n)/n}}, \quad (51)$$

where n denotes the plastic strain hardening exponent of the matrix. After differentiating, one obtains

$$\frac{\partial F}{\partial D_p} \delta D_p + \frac{\partial F}{\partial Y} \delta Y + \frac{\partial F}{\partial p} \delta p = 0. \quad (52)$$

Solving this above linear equation, we have

$$\delta D_p = -\frac{A}{B} \delta Y \frac{C}{B} \delta p, \quad (53)$$

where

$$A = \frac{\partial F}{\partial Y} = -\frac{1}{S_0} (D_p^{cr} - D_p)^{\frac{\alpha-1}{\alpha}} \frac{\Delta p}{p^{(2+n)/n}}, \quad (54)$$

$$B = \frac{\partial F}{\partial D_p} = 1 + \frac{Y}{S_0} (D_p^{cr} - D_p)^{\frac{-1}{\alpha}} \frac{\Delta p}{p^{(2+n)/n}}, \quad (55)$$

$$C = \frac{\partial F}{\partial p} = -\frac{Y}{S_0} (D_p^{cr} - D_p)^{\frac{\alpha-1}{\alpha}} \frac{1 - \Delta p/p}{p^{(2+n)/n}}. \quad (56)$$

Then, the derivative of plastic damage respect to the strain tensor can be rewritten as

$$\frac{\partial D_p}{\partial \epsilon_{kl}} = -\frac{A}{B} \frac{\partial Y}{\partial \epsilon_{kl}} - \frac{C}{B} \frac{\partial p}{\partial \epsilon_{kl}}. \quad (57)$$

Differentiating yield function in Eq. (26) and solving for δp , one obtains

$$\delta p = \frac{\delta \tilde{\sigma}_{eq}^{tr}}{3G + h(p)}. \quad (58)$$

In the J_2 theory, the derivative of trial Mises stress respect to the strain tensor is

$$\frac{\partial \tilde{\sigma}_{eq}^{tr}}{\partial \epsilon_{kl}} = 2G \cdot \eta_{kl}, \quad (59)$$

where η_{kl} is flow direction and can be evaluated as

$$\eta_{kl} = \frac{3\tilde{\sigma}_{ij}^{tr}}{2\tilde{\sigma}_{eq}^{tr}}. \quad (60)$$

Then, we have

$$\frac{\partial p}{\partial \epsilon_{kl}} = \frac{2G \cdot \eta_{kl}}{3G + h(p)}. \quad (61)$$

With Eq. (49) and Eq. (50), the derivative of plastic damage respect to the strain tensor can be directly evaluated

$$\frac{\partial Y}{\partial \epsilon_{kl}} = \frac{\partial Y}{\partial \epsilon_{mn}^e} \frac{\partial \epsilon_{mn}^e}{\partial \epsilon_{kl}} \quad (62)$$

The derivative of the effective stress tensor respect to the strain tensor based on the J_2 plasticity theory is [35]

$$\frac{\partial \tilde{\sigma}_{ij}}{\partial \epsilon_{kl}} = (K - \frac{2}{3}B^*)\delta_{ij}\delta_{kl} + 2B^*\delta_{ik}\delta_{jl} + (\frac{3G \cdot h(p)}{3G + h(p)} - 3B^*)\frac{4}{9}\eta_{ij}\eta_{kl} \quad (63)$$

with $B^* = G(\sigma_y + h(p) \cdot \Delta p)\tilde{\sigma}_{eq}^{tr}$.

Appendix B: Repeatability of the proportional tension-torsion tests

The repeatability of the tests under proportional loadings are shown in Fig. 20. For each loading path, two specimens were used to conduct the testing.

References

- [1] R. K. Abu Al-Rub, S.-M. Kim. Computational applications of a coupled plasticity-damage constitutive model for simulating plain concrete fracture. *Engineering Fracture Mechanics* 77 (2010) 15771603.
- [2] I. Barsoum, J. Faleskog. Rupture mechanisms in combined tension and shear Experiments. *International Journal of Solids and Structures* 44 (2007) 17681786.
- [3] P. Beiss. Pulvermetallurgische Fertigungstechnik. *Springer* (2010).
- [4] J. Besson. Continuum models of ductile fracture: A review. *International Journal of Damage Mechanics* 19 (2010) 352.
- [5] N. Bonora. A nonlinear CDM model for ductile failure. *Engineering Fracture Mechanics* 58 (1997) 1128.
- [6] N. Bonora, D. Gentile, A. Pirondi, G. Newaz. Ductile damage evolution under triaxial state of stress: theory and experiments. *International Journal of Plasticity* 21 (2005) 9811007.
- [7] M. Brünig, S. Gerke, V. Hagenbrock. Micro-mechanical studies on the effect of the stress triaxiality and the Lode parameter on ductile damage. *International Journal of Plasticity* 50 (2013) 4965.
- [8] T.-S. Cao, J.-M. Gachet, P. Montmitonnet, P.-O. Bouchard. A Lode-dependent enhanced Lemaitre model for ductile fracture prediction at low stress triaxiality *Engineering Fracture Mechanics* 124125 (2014) 8096.
- [9] T.-S. Cao, M. Mazière, K. Danas, J. Besson. A model for ductile damage prediction at low stress triaxialities incorporating void shape change and void rotation *International Journal of Solids and Structures* 63 (2015) 240263. .
- [10] S. Carabajar, C. Verdu, R. Fougères. Damage mechanisms of a nickel alloyed sintered steel during tensile tests. *Materials Science and Engineering: A* 232 (1997) 8087.
- [11] S. Castagne, A. Habraken, S. Cescotto. Application of a damage model to an aluminum alloy. *International Journal of Damage Mechanics* 12(2003) 530.
- [12] J. Cedergren, S. Melin, P. Lidström. Numerical modelling of P/M steel bars subjected to fatigue loading using an extended Gurson model. *European Journal of Mechanics - A/Solids* 23(2004) 899908.

- [13] N. Chawla, B. Jester, D. Vonk. Bauschinger effect in porous sintered steels. *Materials Science and Engineering: A* 346 (2003) 266272.
- [14] N. Chawla, X. Deng. Microstructure and mechanical behavior of porous sintered steels. *Materials Science and Engineering: A* 390 (2005) 98112.
- [15] J. Chen, H. Yuan, M. Schneider. Investigation of micromechanical deformation mechanisms in sinter powder metals. *Advanced Material Research*, 668 (2013), 351355.
- [16] U. Cicekli, G.Z. Voyiadjis, R.K. Abu Al-Rub. A plasticity and anisotropic damage model for plain concrete. *International Journal of Plasticity* 23 (2007) 18741900.
- [17] K. Danas, P. Ponte Castañeda. A finite-strain model for anisotropic viscoplastic porous media: I Theory. *European Journal of Mechanics - A/Solids* 28 (2009) 387401.
- [18] X. Deng, G.B. Piotrowski, J.J. Williams, N. Chawla. Effect of porosity and tension-compression asymmetry on the Bauschinger effect in porous sintered steels. *International Journal of Fatigue*, 27 (2005) 12331243
- [19] R. Desmorat, S. Cantournet. Modeling microdefects closure effect with isotropic/anisotropic damage. *International Journal of Damage Mechanics* 17 (2007) 6596.
- [20] V. D. da Silva. A simple model for viscous regularization of elasto-plastic constitutive laws with softening. *Communications in Numerical Methods in Engineering* 20 (2004) 547568
- [21] H. Egner, B. Skoczen. Ductile damage development in two-phase metallic materials applied at cryogenic temperatures. *International Journal of Plasticity* 26 (2010) 488506.
- [22] F. Fritzen, S. Forest, T. Böhlke, D. Kondo, T. Kanit. Computational homogenization of elasto-plastic porous metals. *International Journal of Plasticity* 29 (2012) 102119
- [23] A.L. Gurson. Continuum Theory of Ductile Rupture by Void Nucleation and Growth: Part I Yield Criteria and Flow Rules for Porous Ductile Media. *Journal of Engineering Materials and Technology* 99(1977) 215
- [24] M. Kabatova, E. Dudrova, A. S. Wronski. Microcrack nucleation, growth, coalescence and propagation in the fatigue failure of a powder metallurgy steel. *Fatigue & Fracture of Engineering Materials & Structures* 32 (2009) 214222.
- [25] G. Kang, Y. Liu, J. Ding, Q. Gao. Uniaxial ratcheting and fatigue failure of tempered 42CrMo steel: Damage evolution and damage-coupled visco-plastic constitutive model. *International Journal of Plasticity* 25 (2009) 838860.
- [26] A. S. Khan, H. Liu. Strain rate and temperature dependent fracture criteria for isotropic and anisotropic metals. *International Journal of Plasticity* 37 (2012) 115.

- [27] J. Lemaitre, R. Desmorat. *Engineering damage mechanics - Ductile, creep, fatigue and brittle failures*, Springer-Verlag, 2005.
- [28] M. Luo, M. Dunand, D. Mohr. Experiments and modeling of anisotropic aluminum extrusions under multi-axial loading, Part II: Ductile fracture. *International Journal of Plasticity* 32-33 (2012) 3658.
- [29] Songyun Ma, Huang Yuan. Damage evolution and modeling of sintered metals under multi-axial loading conditions. *Computational Materials Science* 80 (2013) 123133
- [30] K. Nahshon, J.W. Hutchinson. Modification of the Gurson model for shear failure. *European Journal of Mechanics A/Solids*. 27 (2008) 117.
- [31] M. S. Niazi, H. H. Wisselink, T. Meinders. Viscoplastic regularization of local damage models: revisited *Computational Mechanics* 51 (2013), 203-216
- [32] X. Pan, H. Yuan. Computational algorithms and applications of element-free Galerkin methods for nonlocal damage models. *Engineering Fracture Mechanics* 77 (2010), 2640-2653
- [33] M. Schneider, H. Yuan. Experimental and computational investigation of cyclic mechanical behavior and damage evolution of Distaloy AE + 0.5% C. *Powder Metallurgy Progress* 11 (2011), 141-148
- [34] M. Schneider, H. Yuan. Experimental and computational investigation of cyclic mechanical behavior of sintered iron. *Computational Materials Science* 57 (2012) 48 58.
- [35] J.C. Simo, T.J.R. Hughes. *Computational inelasticity*. Springer (1998) New York.
- [36] C. M. Sonsino. Fatigue design principles for sintered steel components. *The Journal of Strain Analysis for Engineering Design* 41 (2006) 497555.
- [37] C. M. Sonsino. Zukunftsperspektiven für die Pulvermetallurgie durch die Betriebsfestigkeit. *Materialwissenschaft und Werkstofftechnik* 37 (2006) 240248.
- [38] G. Straffelini, V. Fontanari. Stress state dependent fracture behaviour of porous PM steels. *Engineering Fracture Mechanics* 78 (2011) 10671076.
- [39] G. Straffelini, A. Molinari. Evolution of tensile damage in porous iron. *Materials Science and Engineering: A* 334 (2002) 96103.
- [40] V. Tvergaard, A. Needleman. Effects of non-local damage in porous plastic solids. *International Journal of Solids and Structures* 32 (1995) 10631077.
- [41] G. Z. Voyiadjis, P. I. Kattan. A Comparative study of damage variables in continuum damage mechanics. *International Journal of Damage Mechanics* 18 (2008) 315340.
- [42] G. Z. Voyiadjis, Z. N. Taqieddin, P. I. Kattan. Anisotropic damageplasticity model for concrete. *International Journal of Plasticity* 24 (2008) 19461965.

- [43] L. Xue. Constitutive modeling of void shearing effect in ductile fracture of porous materials. *Engineering Fracture Mechanics* 75 (2008) 33433366.
- [44] L. Xue, T. Wierzbicki. Ductile fracture initiation and propagation modeling using damage plasticity theory. *Engineering Fracture Mechanics* 75 (2008) 32763293.
- [45] H. Yuan, J. Chen, K. Krompholz, F.H. Wittmann. Investigations of size effects in tensile tests based on a nonlocal micro-mechanical damage model. *Computational Materials Science* 26 (2003) 230-243
- [46] A. Zafari, P. Beiss. Effect of tensile mean stresses on fatigue strength of fe-cu-c steels in as-sintered and heat treated conditions. *Powder Metallurgy Progress* 8 (2008) 200209.

Table 1

Summary of the material model parameters for the sintered iron

Elasto-plastic material properties:		
$E_0 = 162000$ MPa;	$\nu = 0.27$;	$\sigma_{y0} = 135$ MPa
$n = 4.714$;	$K = 549$ MPa	
Elastic damage evolution law:		
$D_b^{sa} = 0.091$;	$b = 19.961$;	$Y_0 = 0.04$ MPa
Plastic damage evolution law:		
$\epsilon_{th} = 0.00038$;	$\alpha = 0.47$;	$S_0 = 334.7$ MPa
$\epsilon_{cr} = 0.12522$;	$D_p^{cr} = 0.205$;	$D^{cr} = 0.296$



Figure 1. Microstructure of the sintered iron ASC.100.29 with the density $7.2\text{g}/\text{cm}^3$.

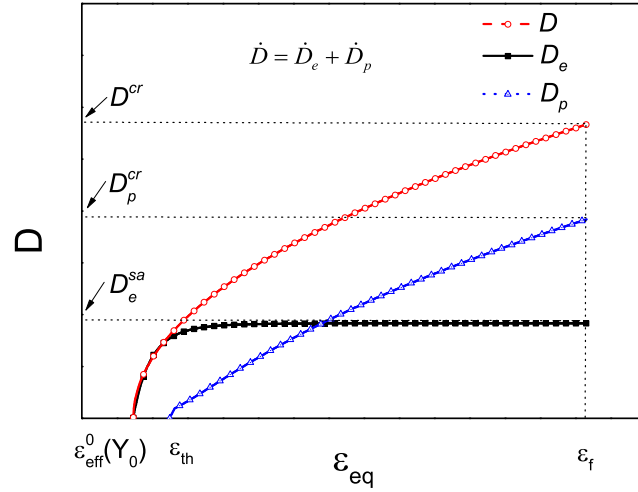


Figure 2. Schematic representation of damage evolution model for the sintered metal. The total damage consists of the elastic damage and plastic damage.

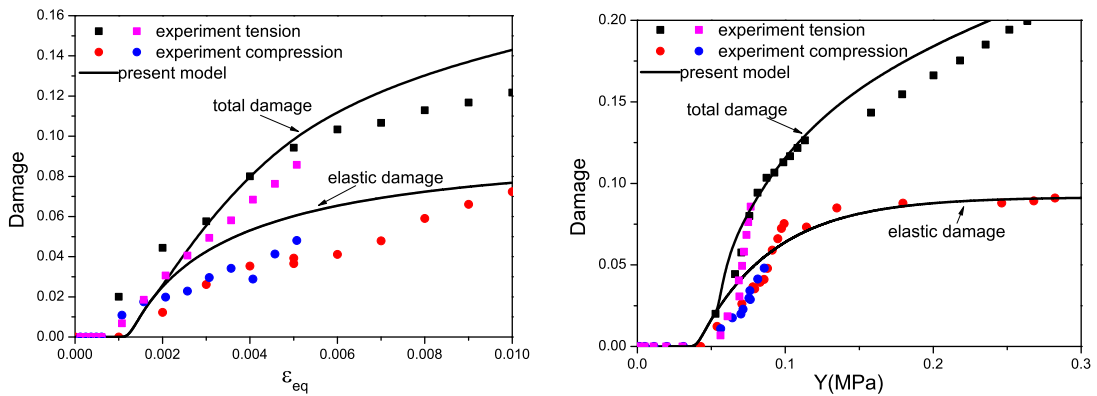


Figure 3. Damage evolution under uniaxial loading conditions: tension and compression. Whereas the damage increases with the tensile loading, the compression causes a material degradation only up to a certain level. (a) Damage as a function of the equivalent strain. (b) Damage as a function of the energy density release rate.

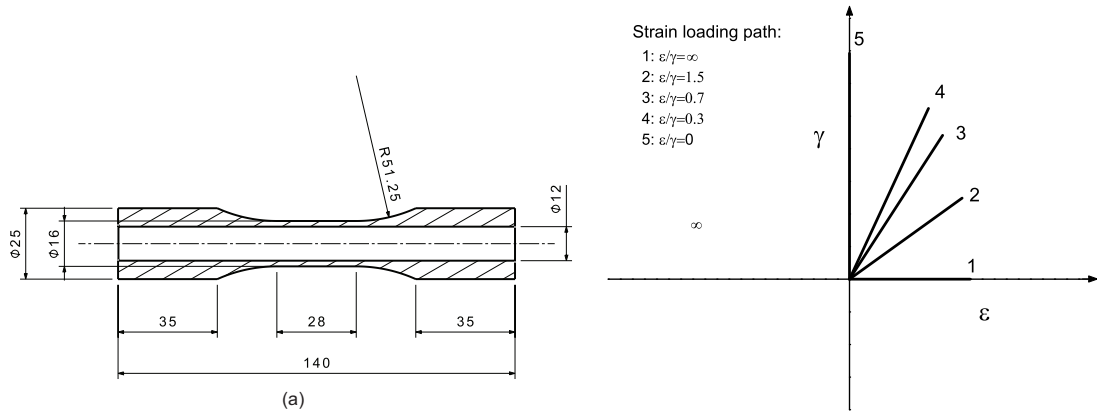


Figure 4. Specimens and proportional loading paths tested in the present work. (a) Geometry of the tubular tension-torsion specimen. (b) Nine different loading paths were used to investigate damage evolution in the sintered iron.

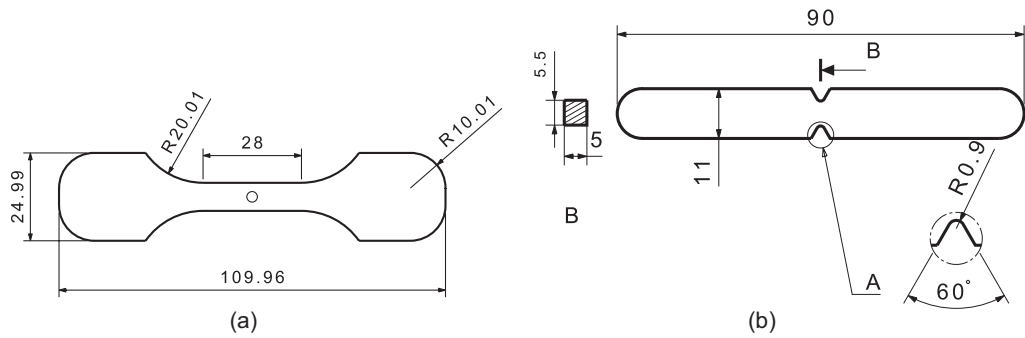


Figure 5. Geometry of specimens used to verify the proposed damage model under complex stress states. (a) Two centre-holed specimens with the hole diameter of 2 and 3mm, respectively. (b) The notched specimen.

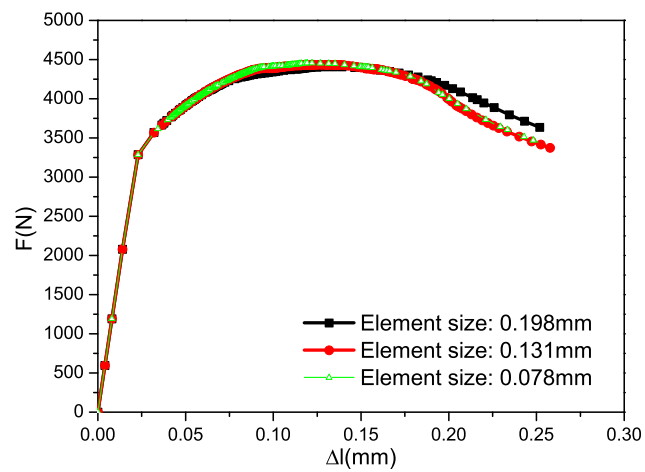


Figure 6. mesh dependency in computations of the holed specimen with the 2 mm diameter.

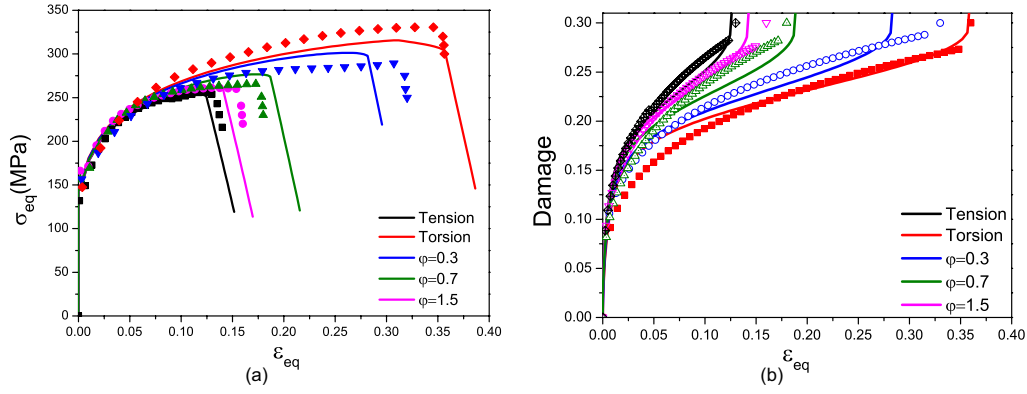


Figure 7. Comparison between experimental results and computational predictions for proportional tension-torsion tests. Symbols denote experimental data and curves are results from the CDM model. (a) Effective stress-strain curves. (b) Damage evolution with effective strain. φ denotes the tension-torsion ratio ϵ/γ between the applied tension and shear strain.

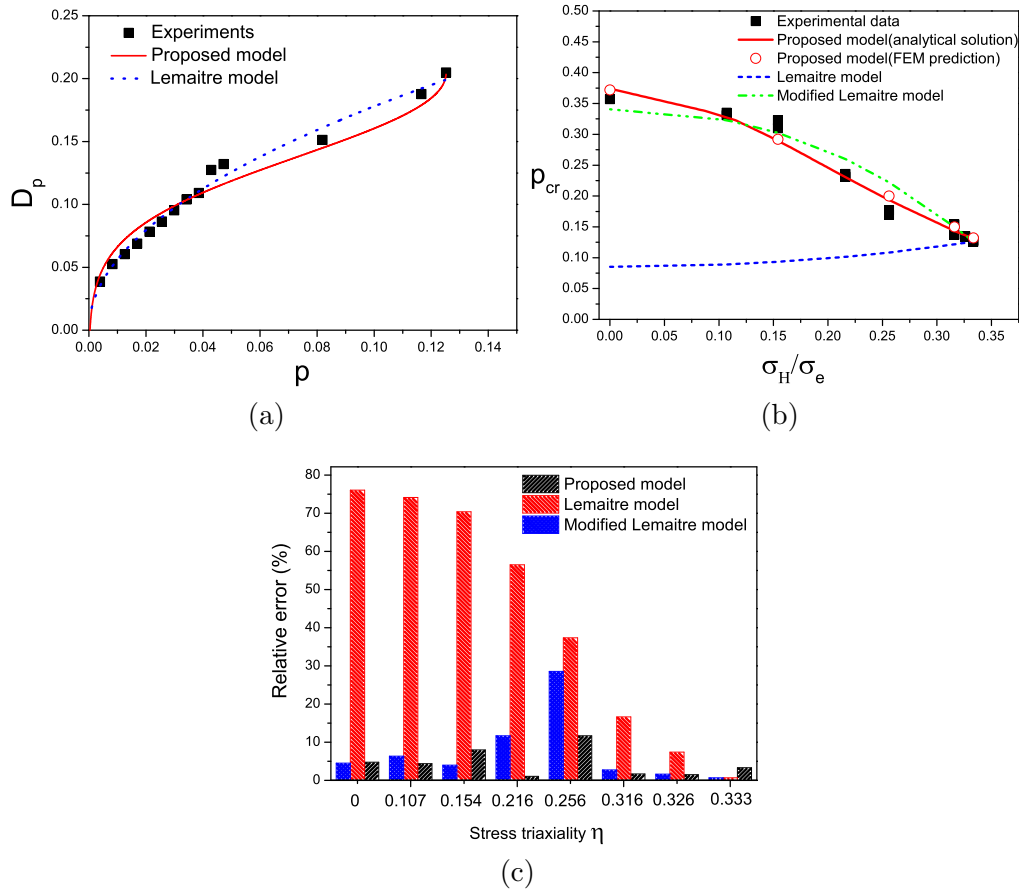


Figure 8. Variations of the fracture strain in tension-torsion specimens under the proportional loading condition. The solid curves are analytical predictions from the CDM model. The symbols denote experiments and computations, respectively.

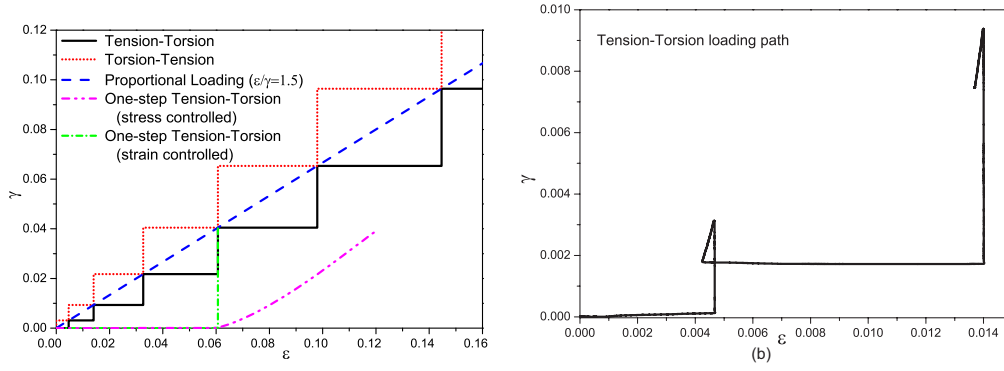


Figure 9. Non-proportional loading paths used to study effects of loading proportionality to the damage evolution. (a) Loading processes of two non-proportional paths (b) Details of small unloading for determining damage evolution in the first two loading cycles. The unloading amplitude keeps constant for the whole tests.

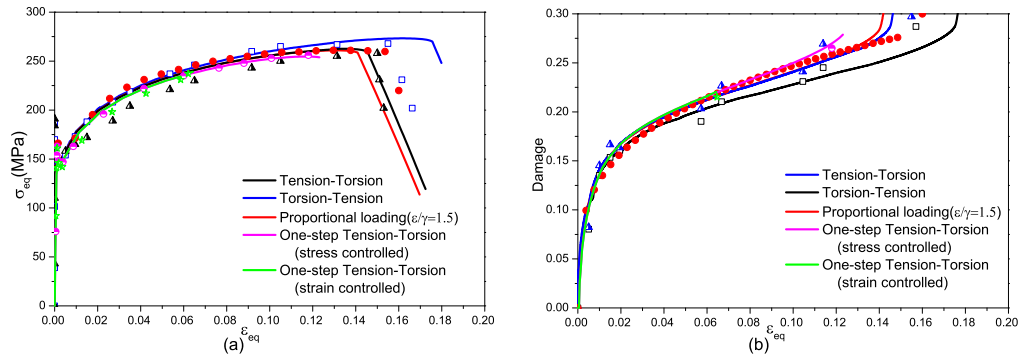


Figure 10. Comparison between experiments and computations for non-proportional tension-torsion loading paths. Symbols denote experimental data and curves are results of computations. (a) Effective stress-strain curves. (b) Damage evolution with effective strain.

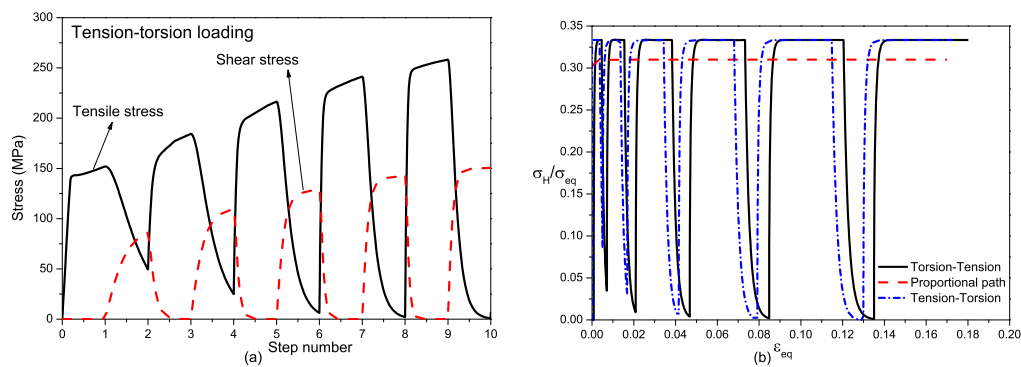


Figure 11. Variations of stresses during the non-proportional loading. (a) The stresses in the tension-torsion loading process. The tension stress and torsion shear stress are in out-of-phase. (b) The stress triaxiality as a function of the equivalent strain for three different loading paths.

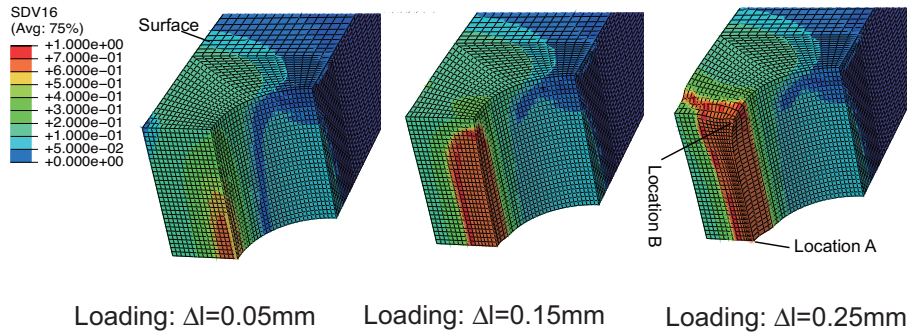


Figure 12. Damage development in the holed specimen (3mm diameter) with increasing load (Δl). The damage initiated near the hole root at the specimen symmetric plane at $\Delta l = 0.05mm$. Then, the damage area propagates through the thickness toward the outer surface of the specimen outside of the symmetric plane, as observed in the experiment.

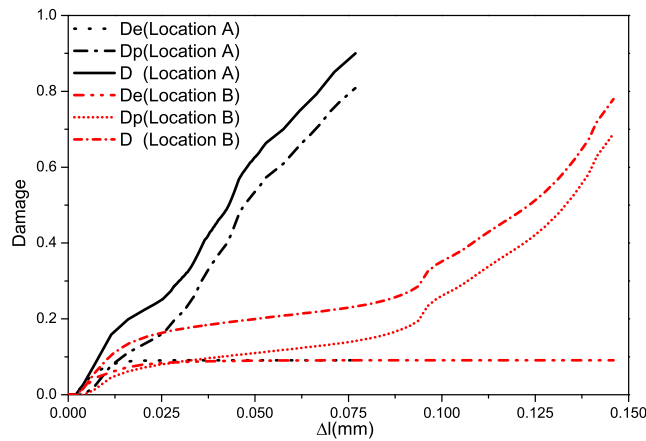


Figure 13. Damage evolution near the middle plane (Location A) and near the free surface of the specimen (Location B), comparing with Figure 12.

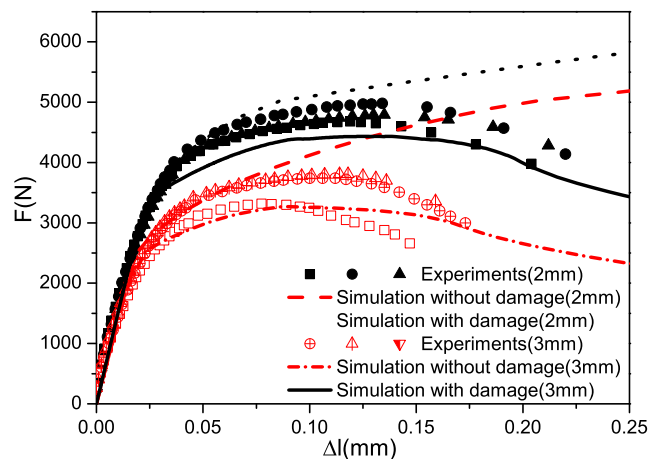


Figure 14. Comparison of load-displacement curves from computations and experiments for the holed specimens with different diameters.

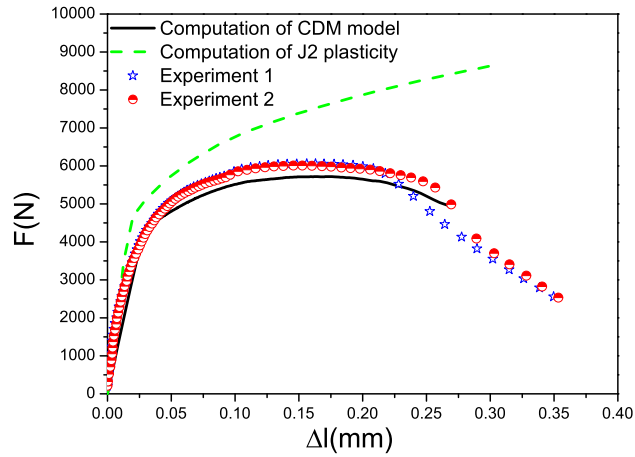


Figure 15. Comparison of load-displacement curves from simulations and experiments for the notched specimen.

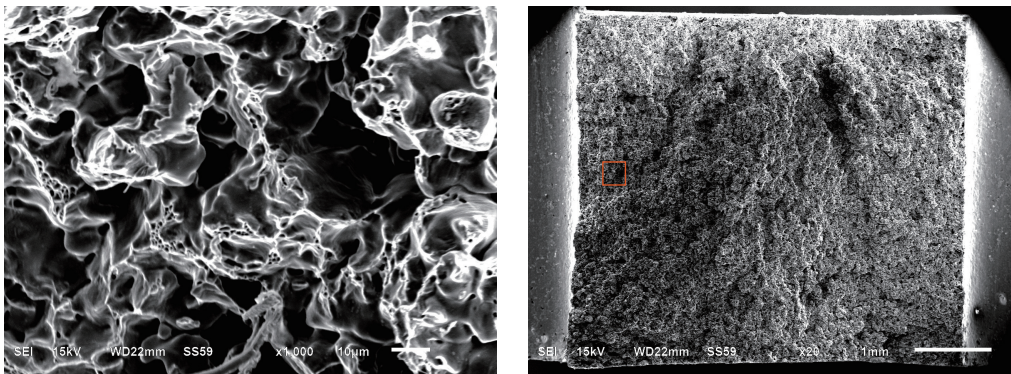


Figure 16. SEM fracture graph of the notched specimen showing the interconnection of ductile dimples in the sintered neck regions leads to the fracture of specimen.

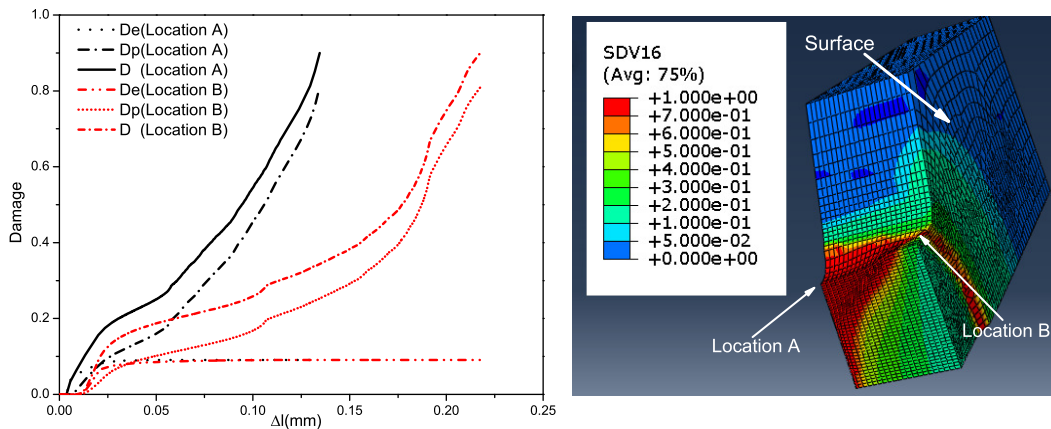


Figure 17. Damage evolution in the computation of notched specimen at two different locations A (near the hole at the specimen middle plane) and B (on the free surface of specimen).

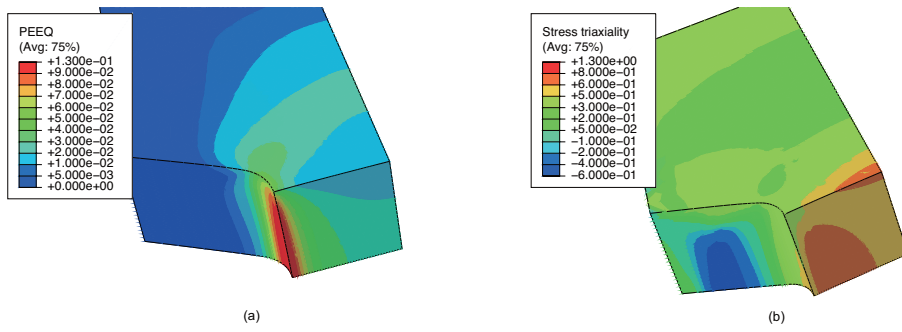


Figure 18. Contour of simulation results without damage effect. (a) effective plastic strain, (b) stress triaxiality.

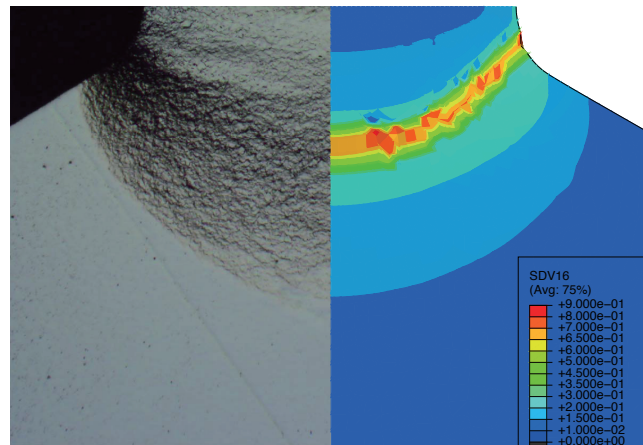


Figure 19. Comparison of damage contour on the free surface between experiment and FEM-simulation

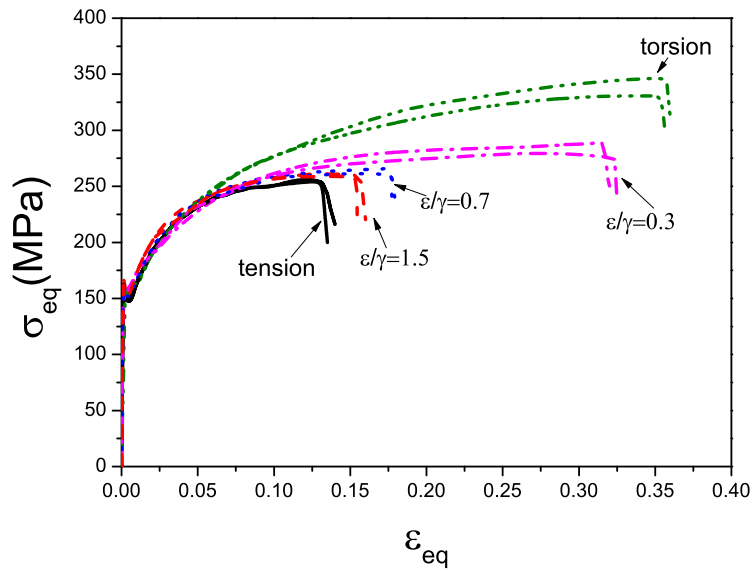


Figure 20. Repeatability of the proportional tension-torsion tests